Article

Ultrahigh-pressure crystallographic passage towards metallic hydrogen

https://doi.org/10.1038/s41586-025-08936-w

Received: 12 September 2024

Accepted: 25 March 2025

Cheng Ji[1,2], Bing Li[1], Jie Luo[3,4], Yongsheng Zhao[1,5], Yuan Liu[3,4], Konstantin Glazyrin[5], Alexander Björling[6], Lucas A. B. Marçal[6,7], Maik Kahnt[6], Sebastian Kalbfleisch[6], Wenjun Liu[8], Yang Gao[1], Junyue Wang[1], Wendy L. Mao[9,10], Hanyu Liu[3,4,11], Yanming Ma[3,4,11], Yang Ding[1], Wenge Yang[1] & Ho-Kwang Mao[1,2]✉

The structural evolution of molecular hydrogen H_2 under multi-megabar compression and its relation to atomic metallic hydrogen is a key unsolved problem in condensed-matter physics. Although dozens of crystal structures have been proposed by theory[1–4], only one, the simple hexagonal-close-packed (*hcp*) structure of only spherical disordered H_2, has been previously confirmed in experiments[5]. Through advancing nano-focused synchrotron X-ray probes, here we report the observation of the transition from *hcp* H_2 to a post-*hcp* structure with a six-fold larger supercell at pressures above 212 GPa, indicating the change of spherical H_2 to various ordered configurations. Theoretical calculations based on our XRD results found a time-averaged structure model in the space group $P\bar{6}2c$ with alternating layers of spherically disordered H_2 and new graphene-like layers consisting of H_2 trimers (H_6) formed by the association of three H_2 molecules. This supercell has not been reported by any previous theoretical study for the post-*hcp* phase, but is close to a number of theoretical models with mixed-layer structures. The evidence of a structural transition beyond *hcp* establishes the trend of H_2 molecular association towards polymerization at extreme pressures, giving clues about the nature of the molecular-to-atomic transition of metallic hydrogen. Considering the spectroscopic behaviours that show strong vibrational and bending peaks of H_2 up to 400 GPa, it would be prudent to speculate the continuation of hydrogen molecular polymerization up to its metallization.

In his Nobel Lecture, Vitaly L. Ginzburg named ‘metallic hydrogen’ and ‘room-temperature superconductor’ as the ‘physical minimum (foundation)’ of the twenty-first century[6]. Metallic and superconducting behaviours[7] of hydrogen are the phenomenological manifestation of its electronic band structure, which is defined by its crystallography. As emphasized by the original Wigner and Huntington (W&H) paper ‘on the possibility of a metallic modification of hydrogen’[8], the metallic conjecture was based on the crystallographic premise of ‘hydrogen atoms on a Bravais lattice’ similar to the body-centred cubic (*bcc*)-structured alkali metals Li and Na. However, the stability of *bcc* atomic hydrogen at any pressure has been dismissed by modern calculations. The true scientific meaning of ‘metallic hydrogen’ is, therefore, the investigation of the pressure-induced crystallographic evolution from molecular hydrogen crystal in a hexagonal close-packed (*hcp*) structure[9,10] to an atomic hydrogen crystal structure that may exhibit exotic behaviours imposed by certain new crystallography. Although multi-megabar electrical conductivity and optical absorption measurements have indicated semi-metallic[11] and probable metallic[12] observations of hydrogen, respectively, thus far the key X-ray diffraction (XRD) measurement, which is necessary for revealing the atomic hydrogen crystal structure, has only disclosed *hcp* or *hcp*-like structures of H_2 molecules (phases I (refs. 9,10), II (refs. 13,14), III (ref. 14) and IV (ref. 15)). Here we report the observation of a post-*hcp* hydrogen crystal structure with 24 H atoms in a hexagonal unit cell.

XRD study of hydrogen samples with submicron grains at multi-megabar pressures is extremely challenging because of the uniquely lowest X-ray scattering cross-section and highest Debye–Waller factor of hydrogen among all elements. Optical Raman and infrared spectroscopies have yielded valuable information on molecular bonding and local symmetry and have been used in the past for identification of ultrahigh-pressure hydrogen phases III (ref. 16), IV (refs. 17,18), IV′ (ref. 19) and V (ref. 20) (Extended Data Fig. 1a). Although optical spectroscopies are not able to define the crystal lattice, they do reveal the important features that the quantum-disordered spherical hydrogen molecules in *hcp* phases I become ‘classically ordered’[21] to show non-zero time average of the molecular bond direction in the

---

[1]Center for High Pressure Science and Technology Advanced Research, Beijing, People’s Republic of China. [2]Shanghai Key Laboratory of Material Frontiers Research in Extreme Environments, Shanghai Advanced Research in Physical Sciences, Shanghai, People’s Republic of China. [3]Key Laboratory of Material Simulation Methods and Software of Ministry of Education, College of Physics, Jilin University, Changchun, People’s Republic of China. [4]State Key Laboratory of Superhard Materials, College of Physics, Jilin University, Changchun, People’s Republic of China. [5]Deutsches Elektronen-Synchrotron, Hamburg, Germany. [6]MAX IV Laboratory, Lund University, Lund, Sweden. [7]Brazilian Synchrotron Light Laboratory, Brazilian Center for Research in Energy and Materials, Campinas, Brazil. [8]Advanced Photon Source, Argonne National Laboratory, Argonne, IL, USA. [9]Department of Earth and Planetary Sciences, Stanford University, Stanford, CA, USA. [10]Stanford Institute for Materials and Energy Sciences, SLAC National Accelerator Laboratory, Menlo Park, CA, USA. [11]International Center of Future Science, Jilin University, Changchun, People’s Republic of China. ✉e-mail: maohk@hpstar.ac.cn

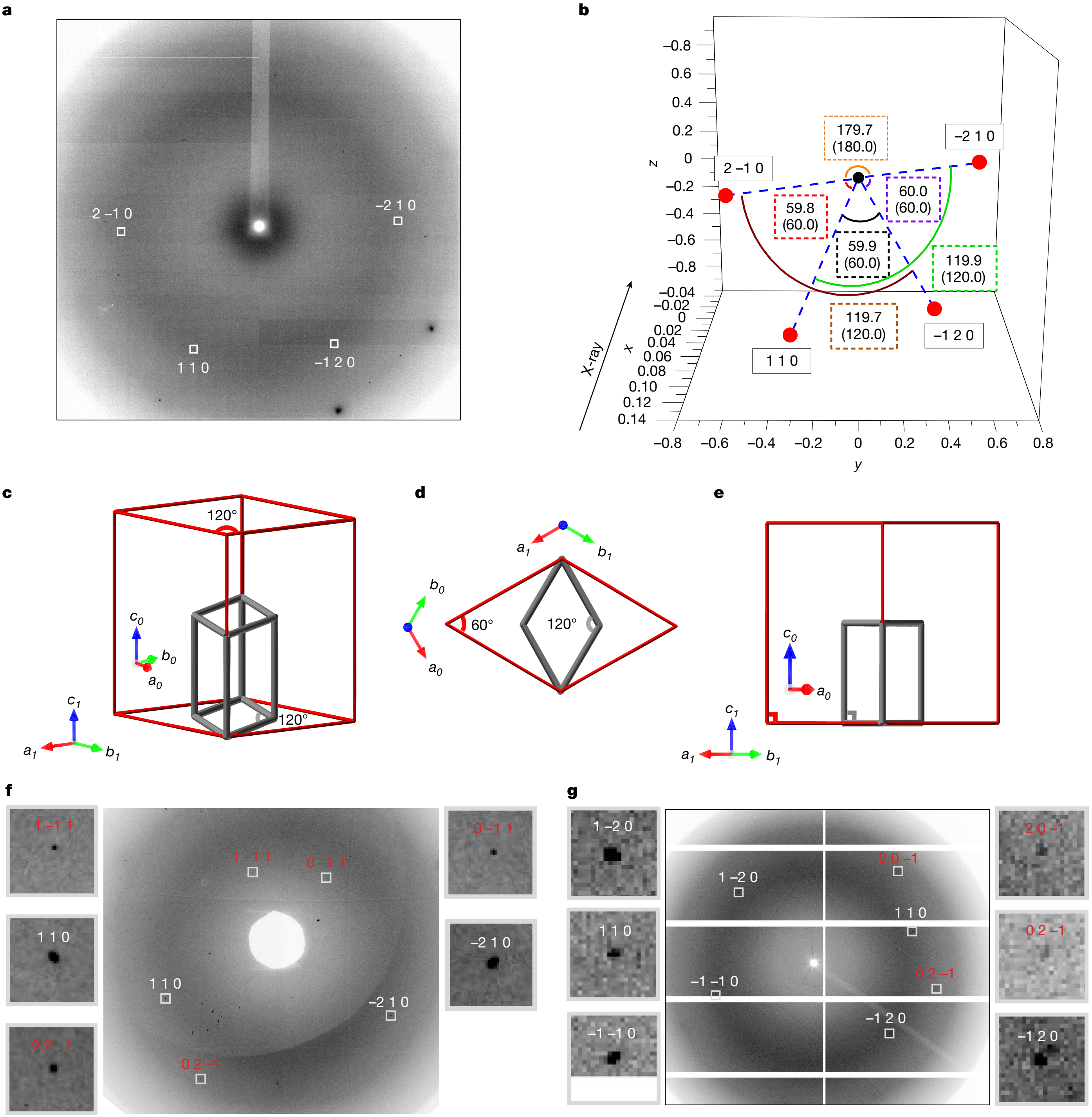

Fig. 1 | Symmetry reflected by SCXRD data and geometrical relationship between *hcp* unit cell and supercell. a, Raw XRD image produced by merging selected step scan frames showing four peaks indexed using √3 × *a* and 2 × *c* supercell at 219 GPa. **b**, Reciprocal space coordinates of the four peaks in **a** and angles between the pairs of peaks. Red and black spheres represent Bragg peaks and reciprocal space origin, respectively. Miller indices are marked beside red spheres in black boxes. Numbers in coloured boxes are the observed angles and theoretical angles (in parentheses). −210, −120, 110 and 2−10 of the supercell correspond to 1−10, 100, 010 and −110 of *hcp*, respectively. Adjacent peaks make angles close to 60.0°, demonstrating the six-fold symmetry. **c**–**e**, The geometrical relationship between the original *hcp* unit cell (grey) and the √3 × *a* 2 × *c* supercell (red); **d** and **e** are projections of **c** along different directions. **f**,**g**, Raw XRD images for data at 245 GPa and 221 GPa, respectively. The XRD images were merged from selected step scan frames. Boxes in XRD images mark the peak positions, with magnified views of the peaks demonstrated on the side in bigger boxes. Numbers are Miller indices in the √3 × *a* 2 × *c* hexagonal supercell. Red indices mark peaks uniquely belonging to the √3 × *a* 2 × *c* hexagonal supercell, whereas white indices mark peaks that are also allowed by the *hcp* symmetry.

higher pressure phases, that is, exhibiting individual H atomic characteristics and orientation ordering in the crystal lattice. Studying this ordering of molecules is an important avenue for understanding the crystallographic evolution of the molecular–atomic hydrogen transitions. A full range of crystal structures, including many different space groups[1,3,4,22–28] and even amorphous superfluid superconductor[29,30]

Table 1 | List of reflections indexed with hexagonal supercell at 221 GPa and 245 GPa

221 GPa, a = 2.9807(3) Å, c = 5.36(1) Å			
h k l	**d_{obs} (Å)**	**d_{cal} (Å)**	**$d_{obs} - d_{cal}$ (Å)**
1 −2 0	1.4885	1.4903	−0.0018
−1 −1 0	1.4901	1.4903	−0.0002
1 1 0	1.4928	1.4903	0.0025
−1 2 0	1.4899	1.4903	−0.0004
2 0 −1	1.2559	1.2547	0.0012
0 2 −1	1.2536	1.2547	−0.0012
245 GPa, a = 2.9374(4) Å, c = 5.243(8) Å			
h k l	d_{obs} (Å)	d_{cal} (Å)	$d_{obs} - d_{cal}$ (Å)
1 −1 1	2.2895	2.2887	0.0008
0 −1 1	2.2887	2.2887	0
−2 1 0	1.4702	1.4687	0.0015
1 1 0	1.4676	1.4687	−0.0011
0 2 −1	1.2358	1.2361	−0.0003

d_{obs} and d_{cal} represent the *d*-spacing values of observed and calculated reflections, respectively. Numbers in parentheses are fitting errors.

have been proposed for the post-*hcp* hydrogen phases, but owing to the inherent difficulties of hydrogen calculations[2], no consensus has yet been reached on structures by calculations; XRD is indispensable.

The frontier of ultrahigh-pressure hydrogen XRD studies has been evolving symbiotically with the new generations of synchrotron X-ray facilities and the development of state-of-the-art micro-diffraction techniques[9,10,15]. Although all available XRD data can be indexed by the *hcp* structure of hydrogen molecules, the *c*/*a* lattice parameter ratio of the *hcp* as a function of pressure shows a distinctive kink at the boundary of phases I and III at 205 GPa and ambient temperature[15], hinting at a probable transition to a post-*hcp* structure because of orientation ordering that would require detection of additional diffraction peaks of much weaker XRD signal intensities. During the past 5 years, we have been continuously improving the single-crystal XRD (SCXRD) technique of hydrogen. Compared with powder XRD, SCXRD has the advantage that the signal for a specific diffraction plane is concentrated at a single spot rather than dispersed along a ring, greatly enhancing the signal-to-background ratio of XRD data. The precise angular relationships among different SCXRD spots also unequivocally define the Miller indices, crystal unit cell and orientation[5,9,10,13]. Furthermore, the strong background was substantially suppressed by using an X-ray transparent composite gasket[15,31]. Using a newly upgraded synchrotron nano-probe[32,33] with a high precision and reproducible sample positioning system[34,35] considerably improves the accuracy and stability of the coordinated sample-beam motion. Overall, these improvements allow us to detect and identify weak reflections that were undetectable previously.

With the improved SCXRD of submicron-sized hydrogen crystals in the phase IV condition, apart from the previously observed (1 0 0),

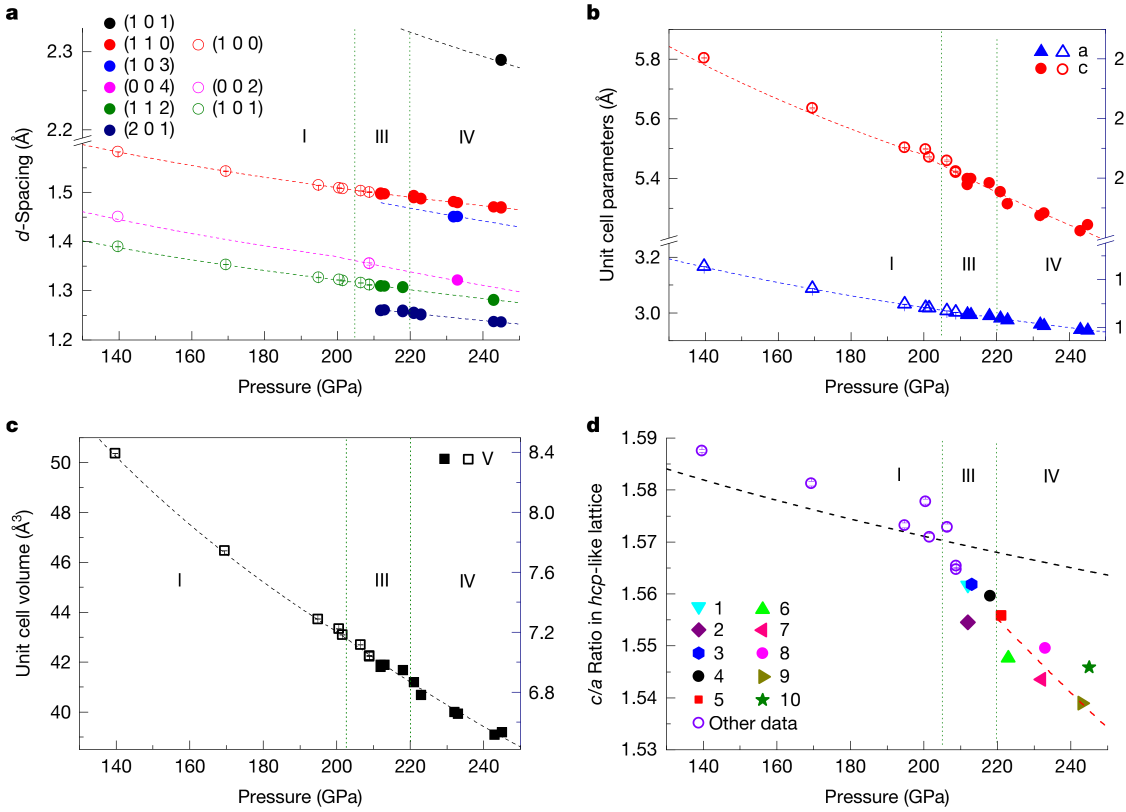

Fig. 2 | Evolution of *d*-spacing and unit cell parameters with pressures. **a**, *d*-Spacing of Bragg peaks. Miller indices for solid and open symbols belong to the supercell and *hcp* unit cell, respectively. Error bar represents standard deviation of the measured *d*-spacing of Bragg peaks within the same class. **b**, Unit cell parameters *a* and *c*. **c**, Unit cell volume. In **a**–**c**, solid and open symbols represent data with and without supercell peaks, respectively. All dashed lines were calculated with the cell parameters reported previously[15], using the relationship $a' = \sqrt{3} \times a$, $c' = 2 \times c$, $V' = 6 \times V$, where a', c', V', a, c and V represent cell parameters of the supercell and *hcp*-like unit cell, respectively. **b** and **c** have double *y*-axes, with the left and right *y*-axes showing the values of the supercell and the *hcp* unit cell, respectively. **d**, *c*/*a* Ratio calculated in a *hcp*-like unit cell. Black and red dashed lines represent the fitting of phase I and phase IV from the previous study[15], respectively. Green dotted lines in all panels mark the reported phase boundaries. Error bars in **a** represent the standard deviation of measured *d*-spacing values. Error bars in **b** and **c** represent fitting errors from the software UnitCell[45], except those for two data points at 232 GPa and 233 GPa, for which the error bars were manually calculated from three Bragg peaks, indexed as −1 −1 0, 1 0 3, 0 −1 3 (232 GPa) and −2 1 0, 1 −1 −3, 0 0 4 (233 GPa), respectively.

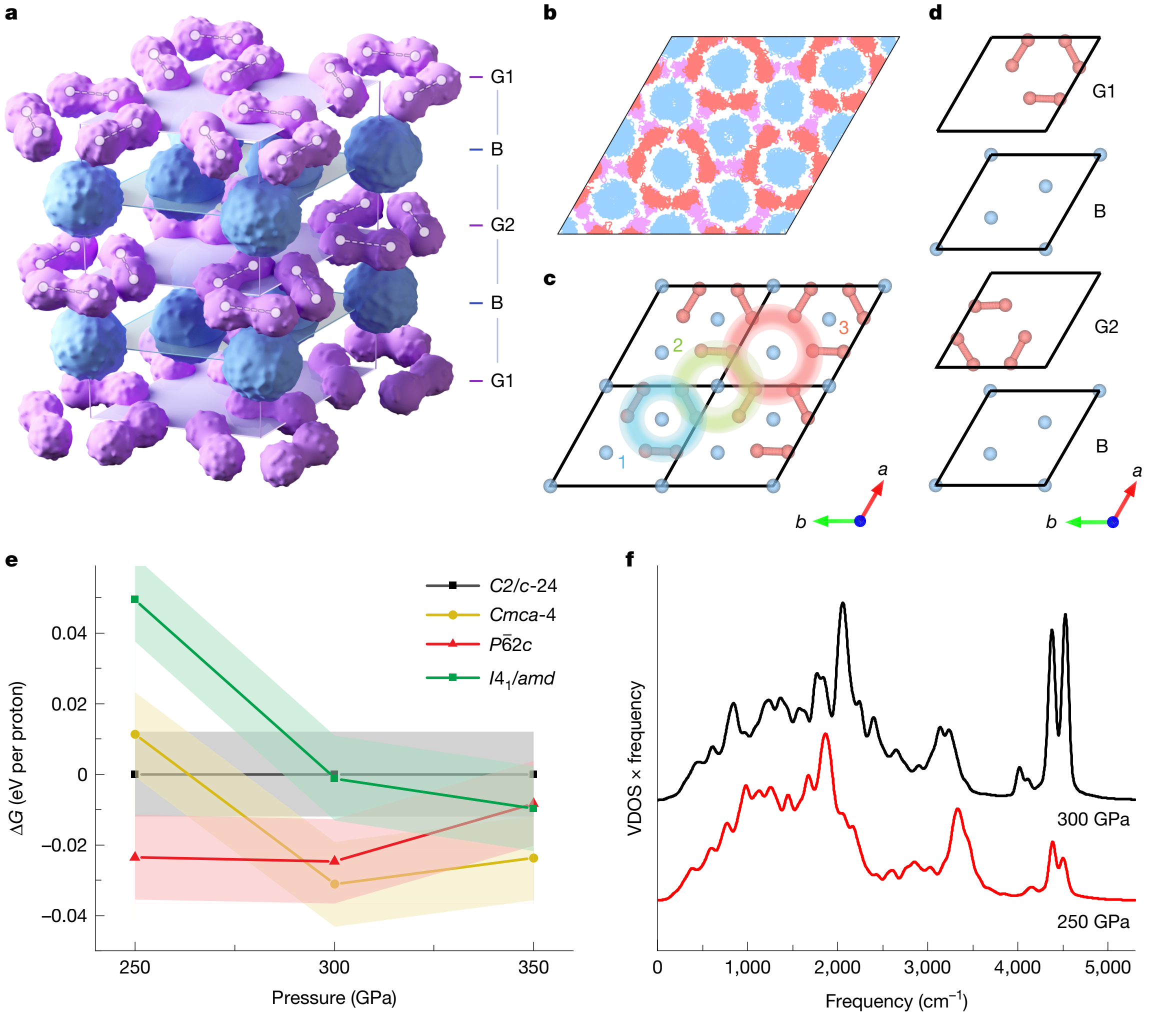

Fig. 3 | Crystal structure demonstration and theoretical calculations of $P\bar{6}2c$ model. a, Schematic of the $P\bar{6}2c$ model. Purple and blue symbols represent hydrogen in G layers and B layers, respectively. Blue spheres in B layers represent freely rotating H_2 molecules. In G1 and G2 layers, white dots and dashed lines represent H atoms and H–H bonds, respectively. **b**, Atomic trajectory of H from MD simulations (4 ps). Red and purple dots represent atomic trajectories in G1 and G2 layers (graphene-like), respectively. Blue dots represent the atomic trajectory in the B layers. **c**, Structural model (4 unit cells correspond to **b**) of $P\bar{6}2c$ containing only G1 and B layers. Red, green and blue circles mark the centre of trimmer units of three different types in G1 layer. **d**, Representation of each layer in one unit cell. **e**, Free energies of the $P\bar{6}2c$, *Cmca*-4 and $I4_1/amd$ structures relative to *C*2/*c*-24 at 300 K using the phonon DOS derived from MD simulations. The shaded region indicates the error range through comparison with results obtained from static phonon calculations. **f**, Vibrational spectra, including all vibrational modes (Raman and infrared), deduced from MD simulations. Calculations at 300 K were also performed, giving similar results compared with those at 100 K but with a lower peak resolution because of temperature effects.

(0 0 2) and (1 0 1) Bragg peaks of the *hcp* unit cell[15] (six-fold symmetry within the *a*–*b* plane is revealed as shown in Fig. 1a,b), we have observed three new weak peaks, indexed as (1 0 1), (1 0 3) and (2 0 1) of a post-*hcp* structure, in 10 different crystal grains at pressures between 212 GPa and 245 GPa (pressure points covered are shown in Extended Data Fig. 1b). None of the new peaks were observed below 212 GPa, clearly marking the boundary between *hcp* and post-*hcp* regions. The angular relationships and *d*-spacings of the three new peaks fit to a hexagonal supercell of the *hcp* cell (within experimental uncertainties), with expanded unit cell parameters of √3 × *a* and 2 × *c*, where *a* and *c* are the original *hcp* unit cell parameters. The geometrical relationship between the new supercell and the *hcp* base cell is shown in Fig. 1c–e. This represents the first direct XRD crystallographic determination of the post-*hcp* structure of hydrogen at ultrahigh pressure. The supercell contains 24 hydrogen atoms per unit cell, whereas the original *hcp* contains 4. The stronger (1 1 0), (0 0 4) and (1 1 2) peaks of the supercell are equivalent to (1 0 0), (0 0 2) and (1 0 1) of the original *hcp* unit cell[15], respectively. The new (1 0 1), (1 0 3) and (2 0 1) peaks are much weaker and require the current technical improvements (apart from the use of X-ray transparent gasket[15,31] as shown in Extended Data Fig. 2c,d) to become visible beyond the background noise.

Two datasets at 245 GPa and 221 GPa are shown in Fig. 1f,g (XRD images) and Extended Data Fig. 3 (rocking curves) to demonstrate the data quality. The quality of indexing using *d*-spacing and reciprocal space angles are demonstrated in Table 1 and Extended Data Table 1, respectively. Similar information on all other SCXRD data can be found in Extended Data Figs. 3 and 4, as well as Extended Data Tables 1 and 2. For the sample at 245 GPa, three weak SCXRD supercell peaks in the (1 0 1) and (2 0 1) classes were observed apart from two SCXRD peaks in the (1 1 0) class (equivalent to *hcp* (1 0 0)), giving $a = 2.9374(4)$ Å, $c = 5.243(8)$ Å and $V = 39.18(6)$ Å^3. Owing to the preferred orientation of hydrogen crystals under compression (*c*-axis of the *hcp* unit cell tends to align with the compression axis) and the limited diamond anvil cell opening, we needed to conduct multiple experiments and search 10 hydrogen crystals to cover the reciprocal space completely, including the rare observations of (0 0 4) (as shown in Fig. 2a and Extended

Table 2 | Structural parameters for the time-averaged $P\bar{6}2c$ model calculated at 250 GPa

Space Group $P\bar{6}2c$ (190)
Lattice parameters
a b c α β γ
2.9069 2.9069 5.2531 90 90 120
Structure parameters
x y z Occupancy Site
1 H 0.3212 0.3512 0.2500 1 6*h*
2 H 0.6592 0.6998 0.2500 1 6*h*
3 H 0.3333 0.6667 0 2 4*f*
4 H 0 0 0 2 2*a*

As H_2 molecules in B layers are constantly rotating freely, their atomic coordinates (H3 and H4) are expressed by their mass centre with occupancy of 2.

Data Fig. 4h). Measured unit cell parameters of the hexagonal post-*hcp* structure are shown in Fig. 2b,c. The large post-*hcp* unit cell allows sufficient degrees of freedom to explain multiple distinctive vibrons in Raman[17,18,36] and infrared[36–39] spectroscopies, indicating at least two chemical environments of hydrogen, in contrast to the single vibron (identical chemical environment) from all H_2 molecules in the original *hcp* unit cell[18].

Based on the XRD observed supercell, we performed DFT-based molecular dynamics (MD) simulations to further explore hydrogen atomic coordinates and quantum motions. A time-averaged structural model in the $P\bar{6}2c$ (190) space group with a mixed structure of alternating Br_2-like (B) and graphene-like (G) layers was obtained. A schematic unit-cell model of the molecular motion in phase IV is shown in Fig. 3a. This model is similar to the previously calculated low symmetry monoclinic *Pc* (ref. 27) and *Cc* (ref. 26) models, and the strong quantum effect makes the time-average unit cell hexagonal. We note that $P\bar{6}2c$ satisfies group–subgroup relation with respect to *hcp* (S.G. $P6_3/mmc$), and we can place all four space groups ($P6_3/mmc$, $P\bar{6}2c$, *Pc* and *Cc*) on the group–subgroup path. In the B layer, the centres of mass of the spherical H_2 molecules are unchanged from the original *hcp* molecular lattice sites (Fig. 3b,c). The G layer consists of a honeycomb formed by H_2 trimer units (Fig. 3c) that contain three H_2 molecules. The honeycomb geometry naturally requires the expansion of the lattice parameter *a* of the *hcp* unit cell with one H_2 unit per layer per unit cell into $\sqrt{3} \times a$ to accommodate one trimer unit per G layer per unit cell (Fig. 3d). The H_2 molecules do not completely dissociate into individual atoms uniformly occupying all triple joints of the honeycomb network, but retain diatomic bonding and orient into at least three distinctive types of trimers: 1, 2 and 3, as marked in Fig. 3c. The variability of the three trimer types provides the distinction of the G1 and G2 layers, resulting in the four-layer ($2 \times c$) G1–B–G2–B unit cell. MD simulations suggest that H_2 molecules in G and B layers exhibit different motions (Fig. 3b). In the G1 and G2 layers, planar rotation of the hexagon H_2 trimmer was disclosed, consistent with a previous report[40]. In the B layers, H_2 molecules rotate about their mass centres in a disordered orientational state, similar to molecules in phase I. This disorder orientational state, also evidenced by the prominent (1 1 0) reflection, is consistent with an entropy-driven phase transition[18] from phase III to phase IV, in which molecular rotations constitute the primary entropy difference[41]. An example of the time-averaged structure model calculated at 250 GPa is shown in Table 2. Simulated XRD pattern based on this time-averaged model agrees with the experimental data, showing all six classes of observed reflections (Extended Data Fig. 6). Free energy and vibrational spectra were also calculated and shown in Fig. 3e,f, which offer additional support for the $P\bar{6}2c$ model. Thus, the $P\bar{6}2c$ model with $\sqrt{3} \times a$ $2 \times c$ supercell of *hcp* is reasonable to represent phase IV, which comprises both unit cell expansion and symmetry reduction. As $P\bar{6}2c$ model exhibits intense quantum effects, a question arises about how the heavier isotope D_2 behaves[42] structurally in phase IV. D_2 does exhibit a slightly different phase boundary between phase III and phase IV, approximately 20 GPa higher than that of H_2 at room temperature[19]. The elevated transition pressure is consistent with the entropy-driven phase transition, which favours H_2 because of its smaller molecular weight. However, the Raman and infrared spectroscopic features of phase IV in the two isotopes are similar, suggesting a similar crystal structure in phase IV of D_2, which awaits further confirmation by SCXRD measurements using the currently reported techniques.

Our SCXRD data support predictions of structural models with mixed structure, as first proposed by Pickard and Needs[1]. The prominent feature of the sharp reduction in *c/a* ratio of the *hcp*-like lattice in both this study (Fig. 2d) and the previous work[15] is consistent to the mixed structure, in which the planar alignment of H_2 molecules in graphene-like layers explains this reduction in *c/a* ratio. Among the numerous theoretically predicted post-*hcp* crystal models of hydrogen[2], some recent models[3,26,27,43] share common features with our $P\bar{6}2c$ model, specifically, *Pc*, *Cc*, $Pca2_1$ (phase V), *BG′BG″* and so on, which also allow all six experimentally observed Bragg peaks. Other models[1,28,43,44] for phases II, III, IV and V, including $Pca2_1$ (phase II), $P2_1/c$, $P6_3/m$, $P6_122$, *Cmca-12*, *Cmca-4*, $BG_xBG_yBG_z$, *Fmmm* and *Ibam* do not satisfy the characteristic supercell peaks with indices (1 0 1), (1 0 3) and (2 0 1), as shown in Extended Data Fig. 7. These predictions open a huge area of investigation awaiting further XRD exploration.

Our results show the key insight of the multi-megabar hydrogen crystallography and stereochemistry. Originally, the metallization of hydrogen was conceptualized as the pressure-induced dissociation of H_2 dimer to form a *bcc* alkali metal[8] of atomic H or even a quantum fluid without spatially ordered atomic structure[29,30]. However, the H_2 dimer in the simple *hcp* lattice was very stable under extreme compression up to 200 GPa. Now we finally observed crystallographic changes in phases III and IV at the pressure range of 212–245 GPa. There is still no sign of intramolecular H–H bond dissociation, but it shows distinctive polymerization by the formation of intermolecular H_2 bonds in the G layers. Considering similar spectroscopic behaviours in IV′ (ref. 19) and V (ref. 20) (up to 400 GPa) that show multiple strong vibrational and bending peaks of hydrogen bonds, it would be prudent to speculate the continuation of polymerization up to metallization. In other words, on further compression, this polymerization process may proceed in various paths with the G layers turning into complete two-dimensional extended sheets such as true graphene, the polymerization of B layers and the polymerization of a three-dimensional extended H network. Thus, the molecular–atomic transition process may not be a dissociation of H_2 molecules into individual H atoms to form a Bravais lattice as W&H proposed[8], nor a transition to complete disordered fluid structures, but more likely an association of H_2 molecules to form an extended H_∞ polymer. When such polymer eventually turns metallic because of J. D. Bernal's all-encompassing view, 'all substances go over under very high pressures into metallic' (as quoted in ref. 8) (ref. 1), it may become a new polymeric metal defined by its crystal structure. The spatially ordered atomic structure opens up opportunities for XRD crystallographic investigation of the molecular–atomic transition. With the rapid progresses of both X-ray sources and high-pressure technology, the ultimate understanding of metallic hydrogen crystallography and consequential exotic properties appears to be within reach.

Online content

Any methods, additional references, Nature Portfolio reporting summaries, source data, extended data, supplementary information, acknowledgements, peer review information; details of author contributions and competing interests; and statements of data and code availability are available at https://doi.org/10.1038/s41586-025-08936-w.

1. Pickard, C. J. & Needs, R. J. Structure of phase III of solid hydrogen. *Nat. Phys.* **3**, 473–476 (2007).
2. McMahon, J. M., Morales, M. A., Pierleoni, C. & Ceperley, D. M. The properties of hydrogen and helium under extreme conditions. *Rev. Mod. Phys.* **84**, 1607–1653 (2012).
3. Monserrat, B. et al. Structure and metallicity of phase V of hydrogen. *Phys. Rev. Lett.* **120**, 255701 (2018).
4. Monacelli, L., Casula, M., Nakano, K., Sorella, S. & Mauri, F. Quantum phase diagram of high-pressure hydrogen. *Nat. Phys.* **19**, 845–850 (2023).
5. Hazen, R. M., Mao, H. K., Finger, L. W. & Hemley, R. J. Single-crystal x-ray diffraction of n-H_2 at high pressure. *Phys. Rev. B* **36**, 3944–3947 (1987).
6. Ginzburg, V. L. Nobel Lecture: on superconductivity and superfluidity (what I have and have not managed to do) as well as on the "physical minimum" at the beginning of the XXI century. *Rev. Mod. Phys.* **76**, 981–998 (2004).
7. Ashcroft, N. W. Metallic hydrogen: a high-temperature superconductor?. *Phys. Rev. Lett.* **21**, 1748–1749 (1968).
8. Wigner, E. & Huntington, H. B. On the possibility of a metallic modification of hydrogen. *J. Chem. Phys.* **3**, 764 (1935).
9. Mao, H. K. et al. Synchrotron X-ray diffraction measurements of single-crystal hydrogen to 26.5 gigapascals. *Science* **239**, 1131–1134 (1988).
10. Loubeyre, P. et al. X-ray diffraction and equation of state of hydrogen at megabar pressures. *Nature* **383**, 702–704 (1996).
11. Eremets, M. I., Drozdov, A. P., Kong, P. P. & Wang, H. Semimetallic molecular hydrogen at pressure above 350 GPa. *Nat. Phys.* **15**, 1246–1249 (2019).
12. Loubeyre, P., Occelli, F. & Dumas, P. Synchrotron infrared spectroscopic evidence of the probable transition to metal hydrogen. *Nature* **577**, 631–635 (2020).
13. Goncharenko, I. & Loubeyre, P. Neutron and X-ray diffraction study of the broken symmetry phase transition in solid deuterium. *Nature* **435**, 1206–1209 (2005).
14. Akahama, Y. et al. Evidence from x-ray diffraction of orientational ordering in phase III of solid hydrogen at pressures up to 183 GPa. *Phys. Rev. B* **82**, 060101 (2010).
15. Ji, C. et al. Ultrahigh-pressure isostructural electronic transitions in hydrogen. *Nature* **573**, 558–562 (2019).
16. Mao, H.-k. & Hemley, R. J. Ultrahigh-pressure transitions in solid hydrogen. *Rev. Mod. Phys.* **66**, 671–692 (1994).
17. Eremets, M. I. & Troyan, I. A. Conductive dense hydrogen. *Nat. Mater.* **10**, 927–931 (2011).
18. Howie, R. T., Guillaume, C. L., Scheler, T., Goncharov, A. F. & Gregoryanz, E. Mixed molecular and atomic phase of dense hydrogen. *Phys. Rev. Lett.* **108**, 125501 (2012).
19. Howie, R. T., Scheler, T., Guillaume, C. L. & Gregoryanz, E. Proton tunneling in phase IV of hydrogen and deuterium. *Phys. Rev. B* **86**, 214104 (2012).
20. Dalladay-Simpson, P., Howie, R. T. & Gregoryanz, E. Evidence for a new phase of dense hydrogen above 325 gigapascals. *Nature* **529**, 63–67 (2016).
21. Mazin, I. I., Hemley, R. J., Goncharov, A. F., Hanfland, M. & Mao, H.-k Quantum and classical orientational ordering in solid hydrogen. *Phys. Rev. Lett.* **78**, 1066–1069 (1997).
22. Nagara, H. & Nakamura, T. Stable phases of solid hydrogen at megabar pressures and at zero temperature. *Phys. Rev. Lett.* **68**, 2468–2471 (1992).
23. Natoli, V., Martin, R. M. & Ceperley, D. Crystal structure of molecular hydrogen at high pressure. *Phys. Rev. Lett.* **74**, 1601–1604 (1995).
24. Johnson, K. A. & Ashcroft, N. W. Structure and bandgap closure in dense hydrogen. *Nature* **403**, 632–635 (2000).
25. Kitamura, H., Tsuneyuki, S., Ogitsu, T. & Miyake, T. Quantum distribution of protons in solid molecular hydrogen at megabar pressures. *Nature* **404**, 259–262 (2000).
26. Liu, H., Zhu, L., Cui, W. & Ma, Y. Room-temperature structures of solid hydrogen at high pressures. *J. Chem. Phys.* **137**, 074501 (2012).
27. Pickard, C. J., Martinez-Canales, M. & Needs, R. J. Density functional theory study of phase IV of solid hydrogen. *Phys. Rev. B* **85**, 214114 (2012).
28. Niu, H. et al. Stable solid molecular hydrogen above 900 K from a machine-learned potential trained with diffusion quantum Monte Carlo. *Phys. Rev. Lett.* **130**, 076102 (2023).
29. Babaev, E., Sudbø, A. & Ashcroft, N. W. A superconductor to superfluid phase transition in liquid metallic hydrogen. *Nature* **431**, 666–668 (2004).
30. Bonev, S. A., Schwegler, E., Ogitsu, T. & Galli, G. A quantum fluid of metallic hydrogen suggested by first-principles calculations. *Nature* **431**, 669 (2004).
31. Ji, C. et al. Crystallography of low Z material at ultrahigh pressure: case study on solid hydrogen. *Matter Radiat. Extremes* **5**, 038401 (2020).
32. Bjorling, A. et al. Ptychographic characterization of a coherent nanofocused X-ray beam. *Opt. Express* **28**, 5069–5076 (2020).
33. Carbone, D. et al. Design and performance of a dedicated coherent X-ray scanning diffraction instrument at beamline NanoMAX of MAX IV. *J. Synchrotron Radiat.* **29**, 876–887 (2022).
34. Johansson, U. et al. NanoMAX: the hard X-ray nanoprobe beamline at the MAX IV Laboratory. *J. Synchrotron Radiat.* **28**, 1935–1947 (2021).
35. Glazyrin, K. et al. Sub-micrometer focusing setup for high-pressure crystallography at the Extreme Conditions beamline at PETRA III. *J. Synchrotron Radiat.* **29**, 654–663 (2022).
36. Goncharov, A. F., Chuvashova, I., Ji, C. & Mao, H. K. Intermolecular coupling and fluxional behavior of hydrogen in phase IV. *Proc. Natl Acad. Sci. USA* **116**, 25512–25515 (2019).
37. Eremets, M. I., Troyan, I. A., Lerch, P. & Drozdov, A. Infrared study of hydrogen up to 310 GPa at room temperature. *High Pressure Res.* **33**, 377–380 (2013).
38. Loubeyre, P., Occelli, F. & Dumas, P. Hydrogen phase IV revisited via synchrotron infrared measurements in H2 and D2 up to 290 GPa at 296 K. *Phys. Rev. B* **87**, 134101 (2013).
39. Zha, C.-S., Liu, Z., Ahart, M., Boehler, R. & Hemley, R. J. High-pressure measurements of hydrogen phase IV using synchrotron infrared spectroscopy. *Phys. Rev. Lett.* **110**, 217402 (2013).
40. Liu, H. & Ma, Y. Proton or deuteron transfer in phase IV of solid hydrogen and deuterium. *Phys. Rev. Lett.* **110**, 025903 (2013).
41. Magdău, I. B. & Ackland, G. J. Identification of high-pressure phases III and IV in hydrogen: Simulating Raman spectra using molecular dynamics. *Phys. Rev. B* **87**, 174110 (2013).
42. Geneste, G., Torrent, M., Bottin, F. & Loubeyre, P. Strong isotope effect in phase II of dense solid hydrogen and deuterium. *Phys. Rev. Lett.* **109**, 155303 (2012).
43. Ackland, G. J. & Loveday, J. S. Structures of solid hydrogen at 300 K. *Phys. Rev. B* **101** 094104 (2020).
44. Monserrat, B., Needs, R. J., Gregoryanz, E. & Pickard, C. J. Hexagonal structure of phase III of solid hydrogen. *Phys. Rev. B* **94**, 134101 (2016).
45. Holland, T. J. B. & Redfern, S. A. T. Unit cell refinement from powder diffraction data: the use of regression diagnostics. *Mineral. Mag.* **61**, 65–77 (1997).

Methods

Experimental

Symmetric DACs were used to generate high pressure, with 30 µm culet size bevelled to 300 µm or 250 µm with an 8.5° bevel angle. Boehler–Almax-type anvils, mostly purchased from Almax easyLab, with 41° X-ray opening, were used to ensure achieving pressures above 200 GPa while gaining reasonable X-ray opening. More than 40 samples were prepared, with data measured in between 140 GPa and 245 GPa. H_2 gas of 99.999% purity was purchased from Chunyu Special Gases. H_2 was pumped to 0.17 GPa and sealed into DAC sample chambers using a gas loading system at HPSTAR, Shanghai. X-ray transparent composite gaskets made by magnesium oxide powder and epoxy mixture[15,31,46] were used for all samples. This gasket provides a clean XRD background, which is important for XRD studies of hydrogen. Sample chambers, originally 10–15 µm in diameter, were fabricated by laser drilling on pre-indented gaskets. Hydrogen samples at high pressure above 200 GPa usually remained about 5 µm in diameter. For most samples, a small piece of gold (Au) flake was loaded inside (or near) a sample chamber to function as a position marker to precisely align the rotation centre. To be consistent, pressure was determined using the hydrogen pressure scale, which we developed previously[15,31].

Synchrotron XRD experiments were attempted at multiple beamlines, including P02.2 (PetraIII, DESY, Germany), NanoMAX (MAX IV Laboratory, Lund University, Sweden), 34-IDE (APS, ANL, USA), and BL15U (SSRF, China). Area detectors and a monochromatic X-ray beam were used at all beamlines. At P02.2 (PetraIII, DESY, Germany), an X-ray probe with 800 nm FWHM at 25 keV, focused by a compound refractive lens, was used. High-precision sample-stage systems were used to couple with the nano-probe setups[35], and this is the key to the success of measuring SCXRD data from individual micron-sized crystal grains of hydrogen. A Pekin Elmer (XRD1621) with a large area was used for recording XRD signals. SCXRD data were also collected by rotating DAC by ±18° by an angular step of 0.1° or 0.2°, with an exposure of 30 s per step. For some samples without Au position markers, two-dimensional scans with the rocking as the fast dimension and horizontal translation as the slow dimension need to be performed to make sure that the XRD signal from a single crystallite can be captured. At the NanoMAX beamline (MAX IV Laboratory, Lund University, Sweden), Kirkpatrick-Baez (KB) mirrors (JTEC, Japan) were used to focus X-rays between 20 keV and 26 keV down to 50–100 nm (FWHM). A Pilatus 1M detector (DECTRIS, Switzerland) was placed about 15 cm downstream of the focus to record XRD images. Data were collected by rotating the sample (DAC) by ±18° in angular steps of 0.1° and 0.2° and using exposure times of 30–60 s per scan point. At 34-ID-E (APS, ANL, USA), a 24 keV X-ray probe with 300 nm FWHM, focused by a JTEC KB mirror pair, was used. A MarCCD165 area detector was used to record the XRD signal. SCXRD data were collected by rotating the DAC by ±18° with an angular step of 0.2° and 30 s to 60 s exposures per angle. We have to emphasize that due to the long data collection time for a single dataset (2–6 h), stability of the beamline setup is crucial for the success of the experiment, including stable hutch temperature. Moreover, as both the crystallite and the X-ray probe are small, a good rotation centre alignment is also important. The current alignment is a two-step procedure. First, rough alignment of the rotation centre by X-ray transmission scan of the Re hole (100–150 µm in diameter) is performed. Second, a fine alignment is done by either a one-dimensional XRD scan across the sample chamber or aligning on Au position markers when available. We strongly recommend loading Au position marker, by the help of which, the precision of rotation centre alignment can be markedly improved (Extended Data Fig. 2). This is important for the SCXRD data collection using nano-probe on samples with micron-sized grains.

For analysing *d*-spacings of Bragg peaks, the raw XRD images were integrated using Dioptas[47] software (PyFAI-based azimuthal integration) and Fityk[48] was used for fitting peak positions. Owing to the limited number of Bragg peaks from a single crystallite, the data processing must be performed manually, instead of using a commercial SCXRD data analysis software. The indexation of SCXRD data is performed in two steps. We first search all peaks that can be indexed into certain crystal grains based on the original *hcp* unit cells. For instance, with an SCXRD dataset, we first searched all possible *hcp* (1 0 0), (0 0 2) and (1 0 1) Bragg peaks, taking reference from the reported EOS[15]. Those peaks are relatively strong, and the search for them lays the basis for indexations in supercell. The reciprocal space coordinates of all searched peaks are then calculated according to the experimental geometries. The angles between each pair of peaks are calculated and compared to the theoretical values based on measured unit cell parameters and the hexagonal lattice. Theoretical angles were calculated as follows:

$$\cos\phi = \frac{h_1h_2 + k_1k_2 + \frac{1}{2}(h_1k_2 + h_2k_1) + \frac{3a^2}{4c^2}l_1l_2}{\sqrt{\left(h_1^2 + k_1^2 + h_1k_1 + \frac{3a^2}{4c^2}l_1^2\right)\left(h_2^2 + k_2^2 + h_2k_2 + \frac{3a^2}{4c^2}l_2^2\right)}} \tag{1}$$

where *a* and *c* are measured unit cell parameters of the *hcp*-like lattice; h_1, k_1, l_1, h_2, k_2 and l_2 are Miller indices of the two peaks for calculating their angle, ϕ, in the reciprocal space. For any pair of peaks, if their angle matches the theoretical value, indexation would be further performed using software Nsingle by inputting a pair of peaks with the corresponding *hcp* Miller indices, as well as the estimated unit cell parameters. Only when one or more predicted peaks based on the UB matrix from indexation were further confirmed by our experimental data, we considered the data to be valid SCXRD data from one crystallite. Typically, the number of peaks found belonging to one crystallite ranges from three to eight. Once a crystallite is confirmed by the above procedure, further indexation by using $\sqrt{3} \times a$ $2 \times c$ supercell would be conducted by assigning the peaks with Miller indices in the supercell. We would then examine whether any predicted peak uniquely belonging to the supercell can be confirmed experimentally. Following these procedures, we found unique supercell peaks in 10 crystal grains.

At present, the SCXRD data show that the three classes of reflections that can be allowed by *hcp* structure ((1 1 0), (0 0 4) and (1 1 2)) are relatively strong, whereas the other three classes uniquely belonging to the supercell ((1 0 1), (1 0 3), (2 0 1)) are relatively weak. However, the intensity information is not appropriate for further quantitative analyses because of intrinsic reasons of the current samples and techniques (micron grains easily shift partially off the submicron beam because of inevitable thermal drift during very long data collection and low number of measurable Bragg peaks inadequate for statistical analyses for removing peaks with abnormal intensity). Further technical advances are thus imperative.

Theoretical calculations

In this work, we performed density functional theory simulations using the VASP code[49]. The exchange correlation function was chosen as Generalized Gradient Approximation Perdew–Burke–Ernzerhof[50] by using the projector-augmented wave method[51]. We choose an energy cutoff of 500 eV and a k-point sampling of $2\pi \times 0.048$ Å^{-1}. The simulated cells of 72 and 96 hydrogen atoms were used. To investigate the dynamics behaviour of hydrogen, we performed isothermal–isobaric (NPT) molecular dynamics (MD) simulations at 250 GPa and 300 K, at which the total run is at least 20,000 steps with a time step of 0.5 fs. As a result of molecular dynamics simulations, together with the MD trajectory (Fig. 3b), it is seen that the simulated structure could be considered as a mixed configuration that contains alternating B and G layers, as reported in previous studies[26,40]. Furthermore, time-averaging centroids of molecular hydrogen units yield a structure with a symmetry space group of $P\bar{6}2c$(190). The detailed information on lattice parameter and atomic position is provided in Table 2.

To explore the impact of quantum nuclear effects on the dynamical behaviour of hydrogen, we performed canonical ensemble (NVT) path-integral molecular dynamics (PIMD) simulations at 250 GPa and 300 K using the PIMD code[52]. The simulated cell containing 96 hydrogen atoms was used. The simulations consisted of a total of 4,000 steps with a time step of 0.5 fs. To sample the imaginary time path integral, 32 beads were used. As a result, the consistency between the MD and PIMD trajectories (Extended Data Fig. 5a,b) indicates that our conclusions remain correct after considering quantum nuclear effects.

We extended our analysis by calculating the phonon density of states (DOS) of $P\bar{6}2c$ using MD simulations. First, we performed 2,000 steps of MD simulations under the NPT/NVT ensemble to obtain the atomic configurations and velocities at finite temperature. Subsequently, more than 3,000 steps of MD simulations were conducted under the microcanonical (NVE) ensemble. After that, the phonon DOS was derived by applying a Fourier transform to the velocity autocorrelation function obtained during the MD simulations under the NVE ensemble. From the phonon DOS, we identified the major Raman and infrared vibron. Two groups of high-frequency peaks (above 3,000 $\mathrm{cm^{-1}}$) were found, corresponding to the double vibron feature in the Raman and infrared experimental data. Furthermore, the softening of the G-layer vibron (3,100–3,500 $\mathrm{cm^{-1}}$) between 250 GPa and 300 GPa is more notable than the B-layer vibron (above 4,000 $\mathrm{cm^{-1}}$), which is also qualitatively consistent with the experiment results (Fig. 3f). Moreover, we further estimated the free energy using the phonon DOS derived from MD simulations at 100 K, the results (Fig. 3e and Extended Data Fig. 5c) indicate that $P\bar{6}2c$ has the lowest energy at 250 GPa.

Data availability

The data that support the findings of this study are available from the corresponding author upon request. Raw SCXRD data are available at Zenodo (https://zenodo.org/uploads/14032134)[53]. Source data are provided with this paper.

46. Ji, C., Li, B., Yang, W. & Mao, H.-k. Crystallographic studies of ultra-dense solid hydrogen. *Chin. J. High Press. Phys.* **34**, 020101 (2020).
47. Prescher, C. & Prakapenka, V. B. *DIOPTAS*: a program for reduction of two-dimensional X-ray diffraction data and data exploration. *High Press. Res.* **35**, 223–230 (2015).
48. Wojdyr, M. *Fityk*: a general-purpose peak fitting program. *J. Appl. Crystallogr.* **43**, 1126–1128 (2010).
49. Kresse, G. & Furthmüller, J. Efficient iterative schemes for ab initio total-energy calculations using a plane-wave basis set. *Phys. Rev. B* **54**, 11169–11186 (1996).
50. Perdew, J. P. et al. Atoms, molecules, solids, and surfaces: applications of the generalized gradient approximation for exchange and correlation. *Phys. Rev. B* **46**, 6671–6687 (1992).
51. Blochl, P. E. Projector augmented-wave method. *Phys. Rev. B* **50**, 17953–17979 (1994).
52. Shiga, M., Tachikawa, M. & Miura, S. Ab initio molecular orbital calculation considering the quantum mechanical effect of nuclei by path integral molecular dynamics. *Chem. Phys. Lett.* **332**, 396–402 (2000).
53. Ji, C. Raw SCXRD data of 'Ultrahigh Pressure Crystallographic Passage Toward Metallic Hydrogen' v.1.0. *Zenodo*. https://doi.org/10.21203/rs.3.rs-5080559/v1 (2025).

Acknowledgements We thank H. Shu for assistance with gas loading systems. We acknowledge financial supports from the National Science Foundation of China (NSFC) 12074014, the National Key Research and Development Program of China 2023YFA1608902 and 2022YFA1402301, the NSFC U2230401, 52288102, 52090024 and T2495233, the Shanghai Science and Technology Committee, China (no. 22JC1410300), the Shanghai Key Laboratory of Material Frontiers Research in Extreme Environments, China (no. 22dz2260800) and the Fundamental Research Funds for the Central Universities. This is also a contribution to the project of Theory of Hydrocarbon Enrichment under Multi-Spheric Interactions of the Earth (THEMSIE04010102). Portions of this work were performed at P02.2, Petra III, Deutsches Elektronen Synchrotron (DESY) in Germany, NanoMAX, MAX IV in Sweden, 34-ID-E, Advanced Photon Source (APS), Argonne National Laboratory (ANL) in the United States, as well as BL15U1, Shanghai Synchrotron Radiation Facility (SSRF) in China. We acknowledge the MAX IV Laboratory for time on Beamline NanoMAX under proposals 20190637, 20220481 and 20230465. Research conducted at MAX IV, a Swedish national user facility, is supported by the Swedish Research Council under contract no. 2018-07152, the Swedish Governmental Agency for Innovation Systems, under contract no. 2018-04969 and Formas under contract no. 2019-02496. This research used resources of the Advanced Photon Source, a US Department of Energy, Office of Science User Facility, operated by Argonne National Laboratory under contract no. DE-AC02-06CH11357.

Author contributions H.-K.M. conceived and supervised the project; C.J., B.L., Y.Z., K.G., A.B., L.A.B.M. and Y.G. performed synchrotron SCXRD measurements; K.G., A.B., M.K., S.K. and W.L. developed and set up the synchrotron nano-probe beamlines; C.J. and J.W. improved the sample preparation techniques for nano-probe SCXRD measurements with C.J. preparing ultrahigh-pressure hydrogen samples; C.J., H.-K.M. and Y.D. performed data analysis; J.L., Y.L., H.L. and Y.M. performed theoretical calculations. H.-K.M., C.J. and W.L.M. wrote the paper in consultation with K.G., L.A.B.M., J.L., H.L. and W.Y.

Competing interests The authors declare no competing interests.

Additional information
Correspondence and requests for materials should be addressed to Ho-Kwang Mao.
Peer review information *Nature* thanks Guoyin Shen and the other, anonymous, reviewer(s) for their contribution to the peer review of this work.
Reprints and permissions information is available at http://www.nature.com/reprints.

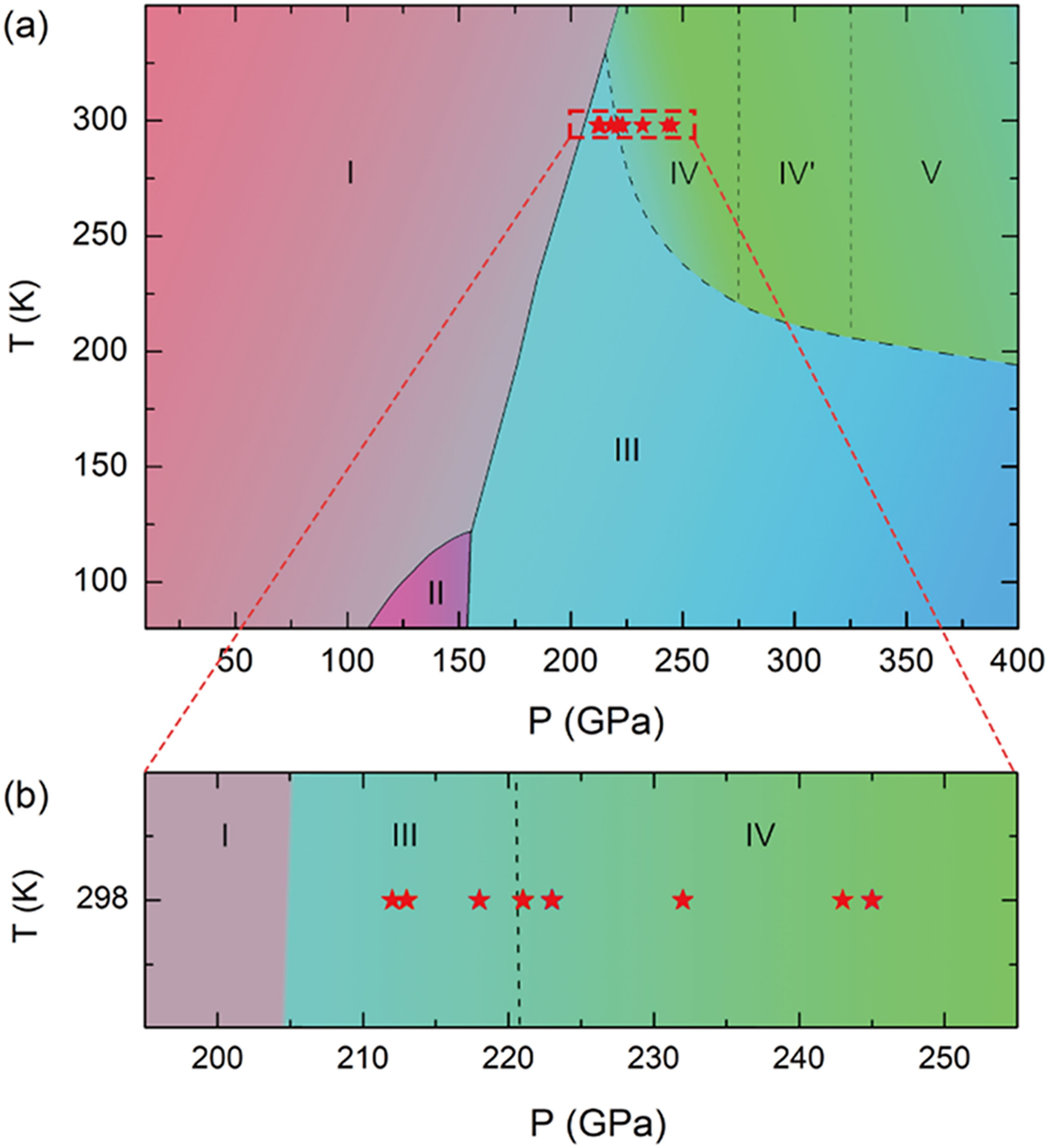

Extended Data Fig. 1 | Post-*hcp* data points in phase diagram. (**a**) Phase diagram of hydrogen. Lines represent phase boundary, stars represent pressure points at which SCXRD data indicate a post-*hcp* structure. All data were collected at room temperature. Similarity in colours of phases IV, IV′, and V represents their similarity in crystal structure as indicated by spectroscopic data. The drawing of this phase diagram takes references of previous studies[11,18,20]. (**b**) Enlarged view of the phase diagram included in the red dash box in (a).

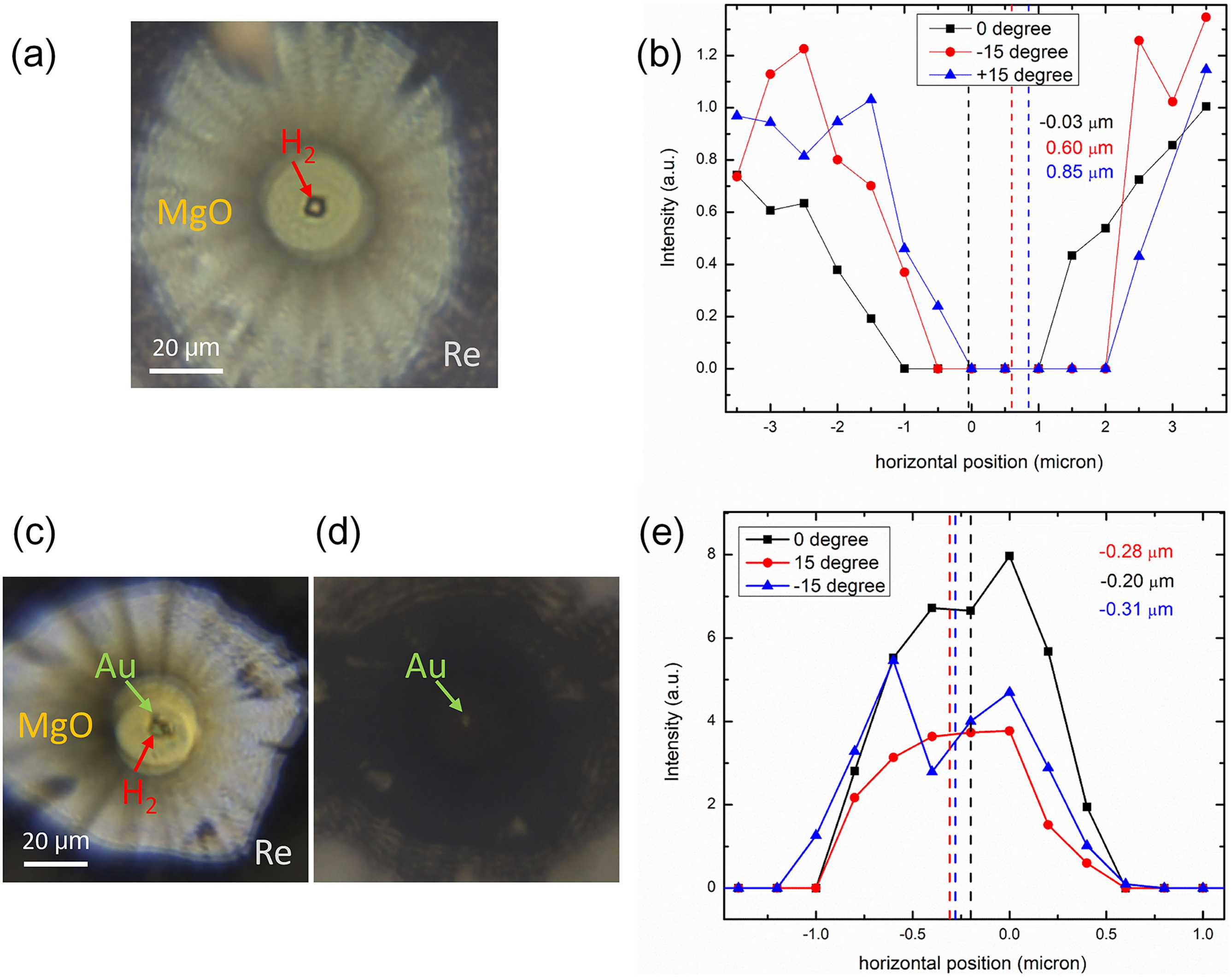

Extended Data Fig. 2 | Qualities of rotation center alignment with and without Au position marker. (**a**) Micro-image of H_2 sealed in MgO-epoxy insert gasket without Au position marker. (**b**) Rotation center alignment by scanning MgO (2 0 0) peak at three different angles. Position with no MgO peak is where H_2 is located. Dash lines mark the center positions of H_2 at different angles. (**c**) and (**d**) show micro-images of H_2 sealed in MgO-epoxy insert gasket with Au position marker with transmitted light and reflected light illumination, respectively. A piece of 2 to 3 μm Au was loaded nearby H_2 sample. (**e**) Rotation center alignment by scanning Au (111) Bragg peak at three different angles. Dash lines mark the center positions of Au at different angles. With Au position marker, the precision of rotation center alignment is substantially improved.

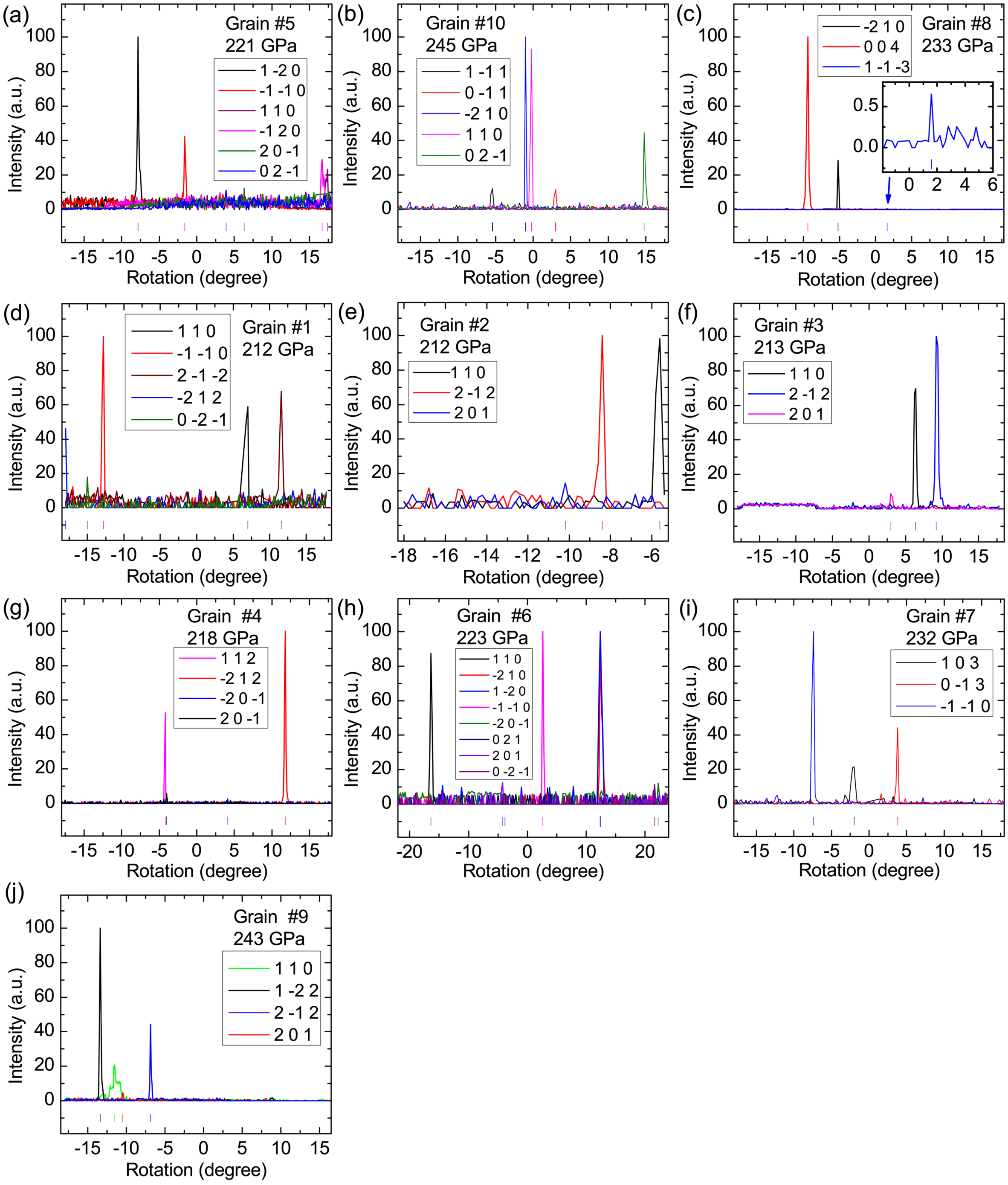

Extended Data Fig. 3 | Rocking curves of Bragg peaks measured in ten crystal grains. (a) and (b) belong to the data measured at 221 GPa and 245 GPa (corresponding to Fig. 1g and f, respectively). (c) to (j) belong to grains #8, #1, #2, #3, #4, #6, #7, and #9 measured at 233 GPa, 212 GPa, 212 GPa, 213 GPa, 218 GPa, 223 GPa, 232 GPa, and 243 GPa, respectively. Such sharp rocking curves are typical for hydrogen at two megabar pressures measured using nano-probe. Miller indexes are in the $\sqrt{3} \times a\,2 \times c$ supercell. In each crystal grain, intensity is normalized against the strongest Bragg peak, of which the value is set to 100.

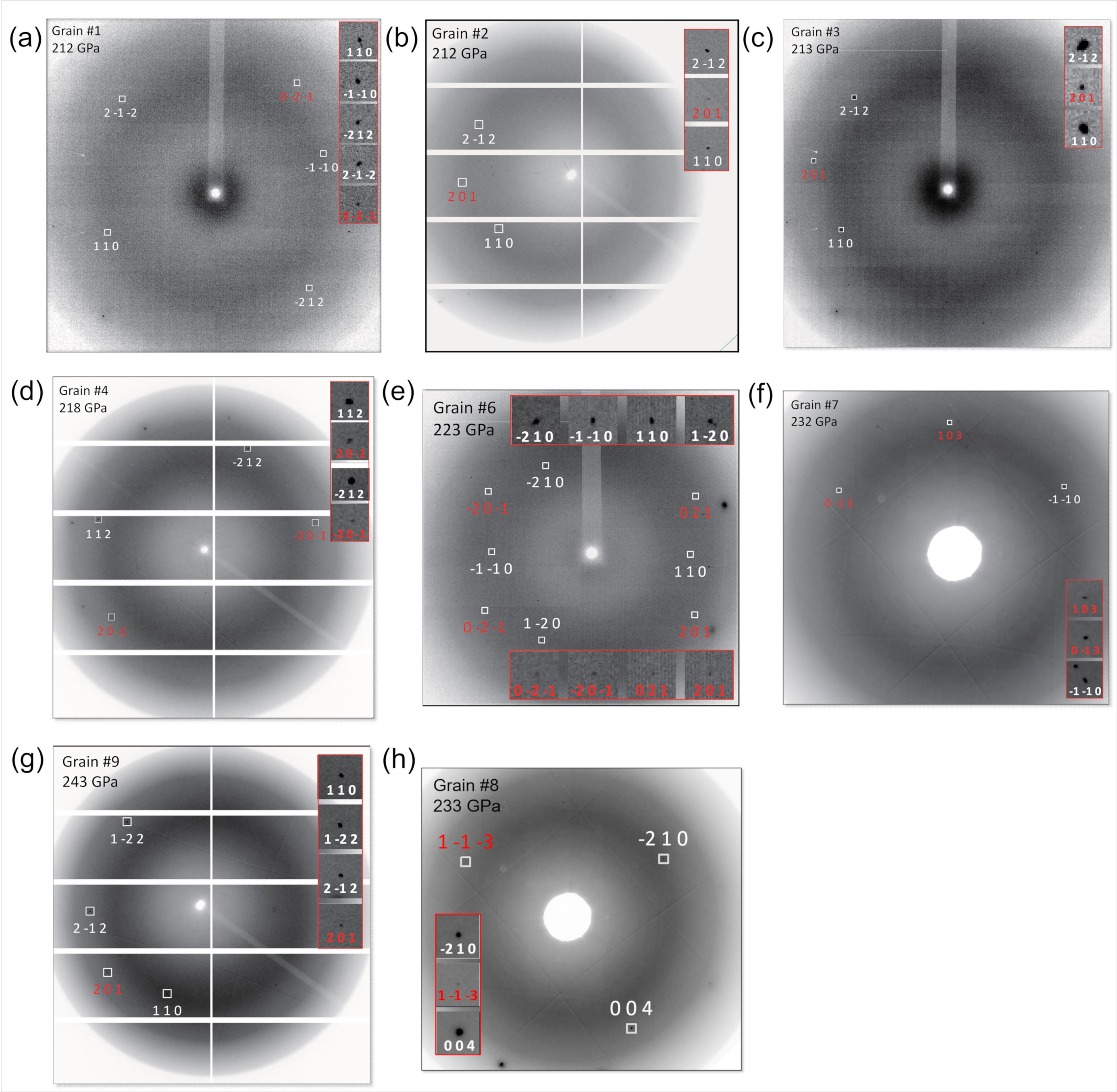

Extended Data Fig. 4 | Raw XRD images of the other seven crystal grains measured at 212 GPa (a), 212 GPa (b), 213 GPa (c), 218 GPa (d), 223 GPa (e), 232 GPa (f), 243 GPa (g), and 233 GPa (h), respectively. Those XRD images were also merged from selected step scan images. Small boxes in XRD images mark the peak positions, with magnified views of the peaks in the red rectangles. Numbers are Miller indices in the $\sqrt{3} \times a\ 2 \times c$ hexagonal supercell. Red indices mark peaks uniquely belonging to the $\sqrt{3} \times a\ 2 \times c$ hexagonal supercell, while white indices mark peaks which are also allowed by the *hcp* symmetry.

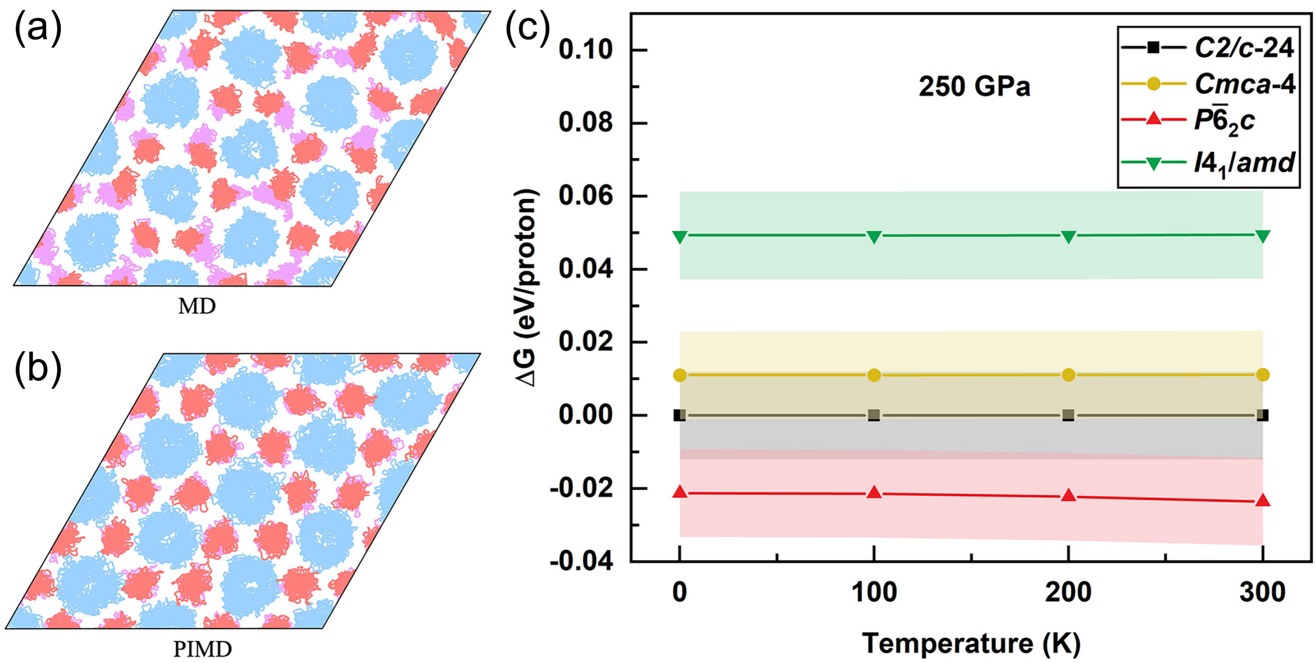

Extended Data Fig. 5 | Atomic trajectories and free energy of $P\bar{6}2c$. (**a**) Atomic trajectory of H from MD simulations with a total time of 2 ps. (**b**) Atomic trajectory of H from PIMD simulations with a total time of 2 ps. Red and purple dots represent atomic trajectory in G1 and G2 layers, respectively. Blue dots represent atomic trajectory in B layers. (c) Free energies of the $P\bar{6}2c$, *Cmca*-4 and $I4_1/amd$ structures relative to *C*2/*c*–24 at 250 GPa using the phonon DOS derived from MD simulations. The shaded region indicates the error range through comparison with results obtained from static phonon calculations.

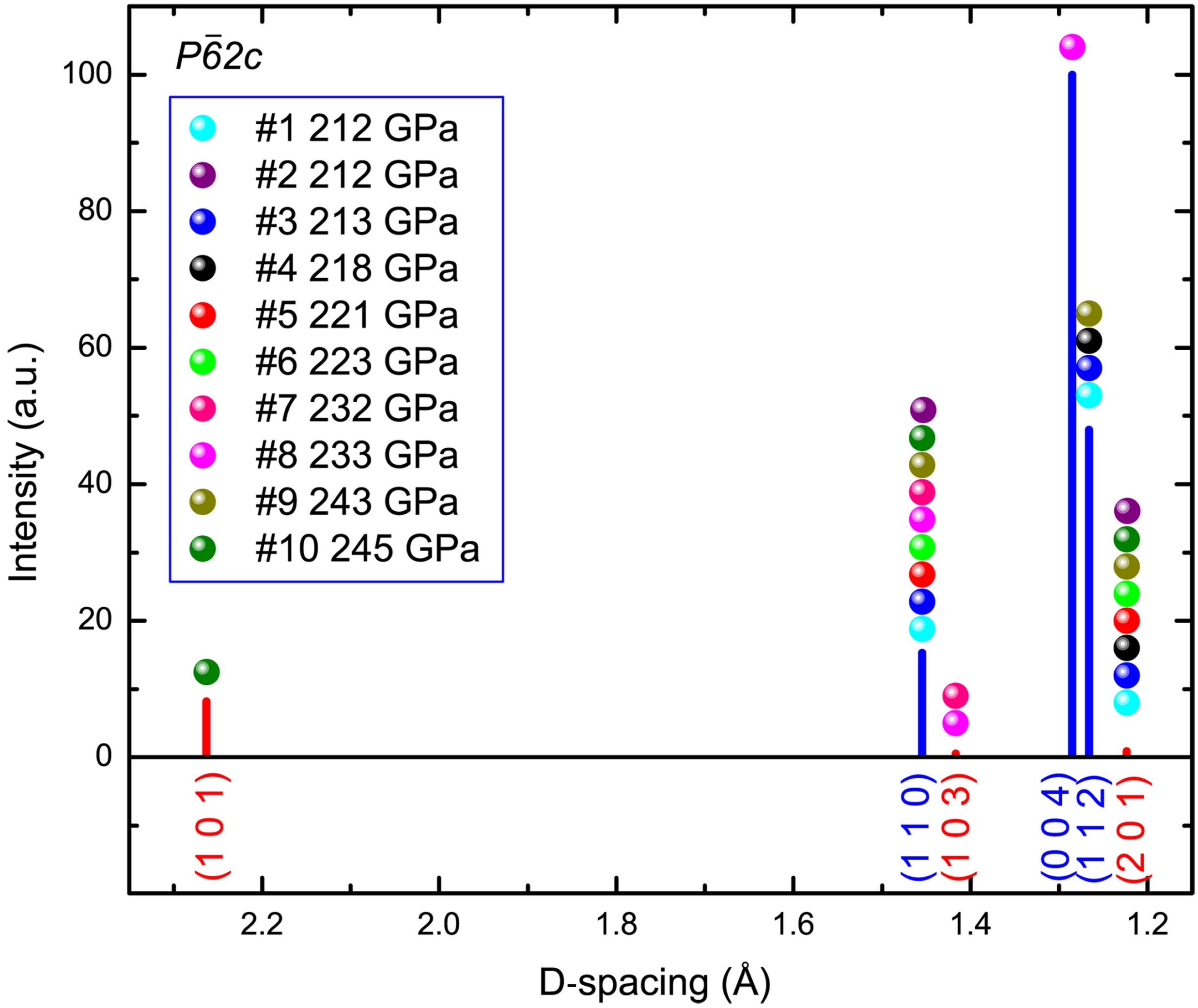

Extended Data Fig. 6 | Simulated XRD pattern based on the *P*$\bar{6}$2*c* model calculated at 250 GPa. Red and blue bars represent calculated intensities. Red bars mark peaks uniquely belonging to the *P*$\bar{6}$2*c* model. Blue bars mark peaks also allowed by the parent *hcp* unit cell. Spheres mark at what pressures the corresponding Bragg peaks were observed. Spheres are only to demonstrate the statistics of observed peaks, and do not reflect the true *d*-spacing of those peaks at their observed pressures.

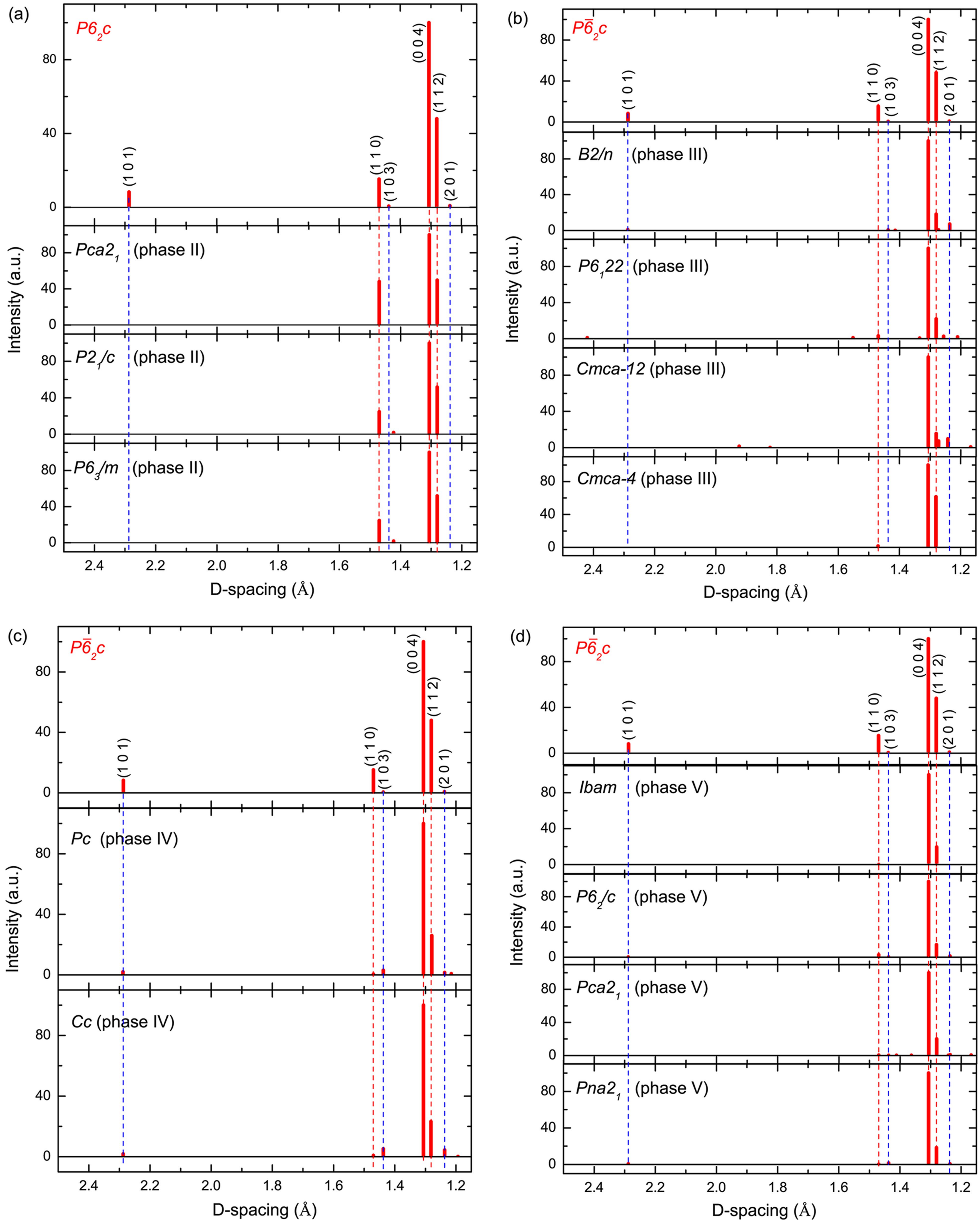

Extended Data Fig. 7 | See next page for caption.

Extended Data Fig. 7 | Comparison of Bragg peaks of different structural models in a *d*-spacing range of 1.15 Å to 2.5 Å to that of $P\bar{6}2c$. Red bars represent intensity of Bragg peaks. Blue dash lines mark unique supercell peaks, red dash lines mark peaks which are also allowed by *hcp*-like unit cell. Intensities of Bragg peaks were calculated by using software PCW. Peak intensity generated by PCW of one peak was divided by the multiplicity of that peak. Unit cell parameters of all models were derived based on *hcp*-like unit cell parameters measured at 245 GPa ($a_0 = 1.6969$ Å and $c_0 = 2.6124$ Å), assuming those lattices being perfect supercell of the *hcp* lattice (in reality, most theoretical models are distorted from the perfect supercell geometry). Specifically, the geometry relationships are listed as the following: $Pca2_1$ (phase II), $a = \sqrt{3}\cdot a_0$ $b = a_0$ $c = c_0$ $\alpha = 90.0°$ $\beta = 90.0°$ $\gamma = 90.0°$; $P6_3/m$ (phase II), $a = 2\cdot a_0$ $b = 2\cdot a_0$ $c = c_0$ $\alpha = 90.0°$ $\beta = 90.0°$ $\gamma = 120.0°$; $P6_122$ (phase III), $a = \sqrt{3}\cdot a_0$ $b = \sqrt{3}\cdot a_0$ $c = 3\cdot c_0$ $\alpha = 90.0°$ $\beta = 90.0°$ $\gamma = 120.0°$; $B2/n$ (phase III), $a = \sqrt{3}\cdot a_0$ $b = 2\cdot c_0$ $c = 3\cdot a_0$ $\alpha = 90.0°$ $\beta = 90.0°$ $\gamma = 90.0°$; $Ibam$ (phase V), $a = \sqrt{3}\cdot a_0$ $b = a_0$ $c = 2\cdot c_0$ $\alpha = 90.0°$ $\beta = 90.0°$ $\gamma = 90.0°$; Pc (phase IV), $a = \sqrt{3}\cdot a_0$ $b = 3\cdot a_0$ $c = 2\cdot c_0$ $\alpha = 90.0°$ $\beta = 90.0°$ $\gamma = 90.0°$; Cc (phase IV), $a = 2\cdot\sqrt{3}\cdot a_0$ $b = 2\cdot\sqrt{3}\cdot a_0$ $c = 2\cdot c_0$ $\alpha = 90.0°$ $\beta = 90.0°$ $\gamma = 120.0°$; $Pca2_1$ (phase V) $a = \sqrt{3}\cdot a_0$ $b = 3\cdot a_0$ $c = 2\cdot c_0$ $\alpha = 90.0°$ $\beta = 90.0°$ $\gamma = 90.0°$; $P6_2/c$ $a = \sqrt{3}\cdot a_0$ $b = \sqrt{3}\cdot a_0$ $c = 2\cdot c_0$ $\alpha = 90.0°$ $\beta = 90.0°$ $\gamma = 120.0°$; $Pna2_1$ (phase V), $a = 2\cdot c_0$ $b = 3\cdot a_0$ $c = \sqrt{3}\cdot a_0$ $\alpha = 90.0°$ $\beta = 90.0°$ $\gamma = 90.0°$. Atomic coordinates of models from literatures[1,26,27,44] were used to calculate XRD patterns. $P6_2/c$ (phase V) in (d) has very weak (1 0 3) peak, which cannot be displayed in the plotted figure. $B2/n$ is another setting of the so-called $C2/c$ structure with *c* axis as the unique axis. The calculated intensity of the reflection corresponding to the (1 1 0) of $P\bar{6}2c$, based on $B2/n$, is 0.

Extended Data Table 1 | Angles between pairs of Bragg peaks in the reciprocal space of the SCXRD data from ten crystal grains

$h_1k_1l_1$	$h_2k_2l_2$	angle$_{obs}$	angle$_{calc}$	Diff.
221 GPa (grain #5)				
1 -2 0	-1 -1 0	60.2	60.0	0.2
1 -2 0	1 1 0	119.5	120.0	-0.5
1 -2 0	-1 2 0	179.3	180.0	-0.7
1 -2 0	2 0 -1	89.8	90.0	-0.2
1 -2 0	0 2 -1	147.1	147.3	-0.4
-1 -1 0	1 1 0	179.6	180.0	-0.4
-1 -1 0	-1 2 0	120.3	120.0	0.3
-1 -1 0	2 0 -1	147.4	147.3	0.1
-1 -1 0	0 2 -1	147.3	147.3	0.0
1 1 0	-1 2 0	59.9	60.0	-0.1
1 1 0	2 0 -1	32.2	32.7	-0.5
1 1 0	0 2 -1	32.8	32.7	0.1
-1 2 0	2 0 -1	89.5	90.0	-0.5
-1 2 0	0 2 -1	32.1	32.7	-0.6
2 0 -1	0 2 -1	58.1	58.2	-0.1
245 GPa (grain #10)				
1 -1 1	0 -1 1	53.2	53.5	-0.3
1 -1 1	-2 1 0	141.0	141.2	-0.2
1 -1 1	1 1 0	90.2	90.0	0.2
1 -1 1	0 2 -1	122.7	122.7	0.0
0 -1 1	-2 1 0	90.0	90.0	0.0
0 -1 1	1 1 0	141.1	141.2	-0.1
0 -1 1	0 2 -1	167.7	167.8	-0.1
-2 1 0	1 1 0	120.1	120.0	0.1
-2 1 0	0 2 -1	90.3	90.0	0.3
1 1 0	0 2 -1	32.5	32.7	-0.2
212 GPa (grain #1)				
1 1 0	-1 -1 0	179.9	180.0	-0.1
1 1 0	-2 1 2	115.9	115.9	-0.0
1 1 0	2 -1 -2	64.1	64.1	0.0
1 1 0	0 -2 -1	147.5	147.3	0.2
-1 -1 0	-2 1 2	64.0	64.1	-0.1
-1 -1 0	2 -1 -2	116.0	115.9	0.1
-1 -1 0	0 -2 -1	32.6	32.6	0.0
-2 1 2	2 -1 -2	179.8	180.0	-0.2
-2 1 2	0 -2 -1	96.4	96.5	-0.1
2 -1 -2	0 -2 -1	83.6	83.5	0.1
212 GPa (grain #2)				
1 1 0	2 -1 2	63.9	64.0	-0.1
1 1 0	2 0 1	32.4	32.6	-0.2
2 -1 2	2 0 1	31.9	31.8	0.1
213 GPa (grain #3)				
1 1 0	2 -1 2	64.1	64.1	0.0
1 1 0	2 0 1	32.6	32.6	0.0
2 -1 2	2 0 1	31.9	31.8	0.0
218 GPa (grain #4)				
1 1 2	-2 1 2	98.4	98.6	-0.2
1 1 2	-2 0 -1	148.1	148.2	-0.1
1 1 2	2 0 -1	51.5	51.3	0.2
-2 1 2	-2 0 -1	51.5	51.3	0.2
-2 1 2	2 0 -1	148.2	148.2	0.0
-2 0 -1	2 0 -1	152.9	153.1	-0.2
223 GPa (grain #6)				
1 1 0	-2 1 0	120.0	119.3	0.7
1 1 0	1 -2 0	120.0	120.7	-0.7
1 1 0	-1 -1 0	180.0	179.5	0.5
1 1 0	-2 0 -1	147.4	146.3	1.1
1 1 0	0 2 1	32.7	32.4	0.3
1 1 0	2 0 1	32.6	33.1	-0.5
1 1 0	0 -2 -1	147.3	148.1	-0.8
-2 1 0	1 -2 0	120.0	120.0	0.0
-2 1 0	-1 -1 0	60.0	60.2	-0.2
-2 1 0	-2 0 -1	32.7	32.6	0.1
-2 1 0	0 2 1	90.0	89.7	0.3
-2 1 0	2 0 1	147.3	147.0	0.3
-2 1 0	0 -2 -1	90.0	89.7	0.3
1 -2 0	-1 -1 0	60.0	59.8	0.2
1 -2 0	-2 0 -1	90.0	90.2	-0.2
1 -2 0	0 2 1	147.3	147.7	-0.4
1 -2 0	2 0 1	90.0	90.4	-0.4
1 -2 0	0 -2 -1	32.7	33.0	-0.3
-1 -1 0	-2 0 -1	32.6	33.2	-0.6
-1 -1 0	0 2 1	147.3	147.2	0.1
-1 -1 0	2 0 1	147.4	147.4	0.0
-1 -1 0	0 -2 -1	32.7	32.2	0.5
-2 0 -1	0 2 1	121.9	121.3	0.6
-2 0 -1	2 0 1	180.0	179.3	0.7
-2 0 -1	0 -2 -1	58.1	58.0	0.1
0 2 1	2 0 1	58.1	58.2	-0.1
0 2 1	0 -2 -1	180.0	179.3	0.7
2 0 1	0 -2 -1	121.9	122.5	-0.6
232 GPa (grain #7)				
1 0 3	0 -1 3	58.8	58.7	0.1
1 0 3	-1 -1 0	60.8	60.7	0.1
0 -1 3	-1 -1 0	119.5	119.4	0.1
233 GPa (grain #8)				
-2 1 0	0 0 4	89.4	90.0	-0.6
-2 1 0	1 -1 -3	118.9	119.4	-0.5
0 0 4	1 -1 -3	145.9	145.5	0.4
243 GPa (grain #9)				
1 1 0	1 -2 2	115.5	115.8	-0.3
1 1 0	2 -1 2	64.6	64.2	0.4
1 1 0	2 0 1	32.8	32.7	0.1
1 -2 2	2 -1 2	50.9	51.6	-0.7
1 -2 2	2 0 1	82.9	83.3	-0.4
2 -1 2	2 0 1	32.0	31.9	01

Two datasets measured at 221 GPa and 245 GPa, corresponding to Table 1 of the main text, are listed at the top of the table. angle$_{obs}$ and angle$_{calc}$ represent experiment and calculation values (°), respectively. Diff. represents angle$_{obs}$ minus angle$_{calc}$. Miller indexes belong to the $\sqrt{3}\times a$ $2\times c$ hexagonal supercell.

Extended Data Table 2 | List of reflections indexed with hexagonal supercell from the other eight crystal grains

212 GPa (grain #1)

h k l	d_{obs} (Å)	d_{cal} (Å)	d_{obs}- d_{cal}
-1 -1 0	1.4974	1.4968	0.0006
-1 1 0	1.4970	1.4968	0.0002
2 -1 2	1.3094	1.3090	0.0004
-2 1 -2	1.3087	1.3090	-0.0003
-2 0 -1	1.2598	1.2604	-0.0006

212 GPa (grain #2)

h k l	d_{obs} (Å)	d_{cal} (Å)	d_{obs}- d_{cal}
1 1 0	1.4980	1.4980	0.0000
2 -1 2	1.3087	1.3087	0.0000
2 0 1	1.2596	1.2612	-0.0015

213 GPa (grain #3)

h k l	d_{obs} (Å)	d_{cal} (Å)	d_{obs}- d_{cal}
1 1 0	1.4967	1.4967	0.0000
2 -1 2	1.3087	1.3087	0.0000
2 0 1	1.2603	1.2603	0.0000

218 GPa (grain #4)

h k l	d_{obs} (Å)	d_{cal} (Å)	d_{obs}- d_{cal}
1 1 2	1.3075	1.3069	0.0006
-2 1 2	1.3063	1.3069	-0.0006
0 2 -1	1.2573	1.2587	-0.0014
0 -2 -1	1.2601	1.2587	0.0014

223 GPa (grain #6)

h k l	d_{obs} (Å)	d_{cal} (Å)	d_{obs}- d_{cal}
1 1 0	1.4865	1.4867	-0.0002
-2 1 0	1.4866	1.4867	-0.0001
1 -2 0	1.4871	1.4867	0.0004
-1 -1 0	1.4867	1.4867	0.0000
0 2 -1	1.2515	1.2513	0.0002
-2 0 -1	1.2513	1.2513	0.0000
0 -2 1	1.2506	1.2513	-0.0007
2 0 -1	1.2519	1.2513	0.0006

232 GPa (grain #7)

h k l	d_{obs} (Å)	d_{cal} (Å)	d_{obs}- d_{cal}
1 1 0	1.4796	1.4796	0.0000
1 0 3	1.4492	1.4498	-0.0006
0 -1 3	1.4504	1.4498	0.0006

233 GPa (grain #8)

h k l	d_{obs} (Å)	d_{cal} (Å)	d_{obs}- d_{cal}
-2 1 0	1.4789	1.4771	0.0018
0 0 4	1.3214	1.3207	0.0007
1 -1 -3	1.4505	1.4505	0.0000

243 GPa (grain #9)

h k l	d_{obs} (Å)	d_{cal} (Å)	d_{obs}- d_{cal}
1 1 0	1.4698	1.4697	0.0001
1 -2 2	1.2803	1.2808	-0.0005
2 -1 2	1.2814	1.2808	0.0006
0 -2 1	1.2365	1.2366	-0.0001

d_{obs} and d_{cal} represent the *d*-spacing values of observed and calculated reflections, respectively. Numbers in parenthesis are errors. For data which possess more than three Bragg peaks, errors are the fitting errors from the software UnitCell[45]. For grain #2, #3, #7, and #8, unit cell parameters *a* and c were calculated using the formula $\frac{1}{d_{hkl}^2} = \frac{4(h^2 + hk + k^2)}{3a^2} + \frac{l^2}{a^2}$ based on a single peak or pairs of peaks. When there is more than one way to calculate one unit cell parameter, error is produced by taking the standard deviation of the calculated values from different combinations. For grain #2, no error is shown since unit cell parameters were calculated using only 1 1 0 and 2 -1 2, because the dspacing of 2 0 1 is considered not reliable (peak intensity is too weak).